

The quantum efficiency and diffractive image artifacts of Si:As IBC mid-IR detector arrays at 5 – 10 μm :
Implications for the *JWST*/MIRI detectors

ANDRÁS GÁSPÁR,¹ GEORGE H. RIEKE,¹ PIERRE GUILLARD,^{2,3} DANIEL DICKEN,⁴ RENÉ GASTAUD,⁴ STACEY ALBERTS,¹
JANE MORRISON,¹ MICHAEL E. RESSLER,⁵ IOANNIS ARGYRIOU,⁶ AND ALISTAIR GLASSE⁷

¹*Steward Observatory and the Department of Astronomy, The University of Arizona, 933 N Cherry Ave, Tucson, AZ, 85750, USA*

²*Sorbonne Université, CNRS, UMR 7095, Institut d'Astrophysique de Paris, 98bis bd Arago, 75014 Paris, France*

³*Institut Universitaire de France, Ministère de l'Éducation Nationale, de l'Enseignement Supérieur et de la Recherche, 1 rue Descartes, 75231 Paris Cedex 05, France*

⁴*AIM, CEA, CNRS, Université Paris-Saclay, Université Paris Diderot, Sorbonne Paris Cité, F-91191 Gif-sur-Yvette, France*

⁵*Jet Propulsion Laboratory, California Institute of Technology, 4800 Oak Grove Drive, Pasadena, CA 91109, USA*

⁶*Institute of Astronomy, Celestijnenlaan 200D - box 2401, 3001 Leuven, Belgium*

⁷*UK Astronomy Technology Centre, Royal Observatory, Edinburgh, Blackford Hill, Edinburgh EH9 3HJ, UK*

(Received November 25, 2020; Revised; Accepted)

Submitted to PASP

ABSTRACT

Arsenic doped back illuminated blocked impurity band (BIBIB) silicon detectors have advanced near and mid-IR astronomy for over thirty years; they have high quantum efficiency (QE), especially at wavelengths longer than 10 μm , and a large spectral range. Their radiation hardness is also an asset for space based instruments. Three examples of Si:As BIBIB arrays are used in the Mid-Infrared Instrument (MIRI) of the James Webb Space Telescope (*JWST*), observing between 5 and 28 μm . In this paper, we analyze the parameters leading to high quantum efficiency (up to $\sim 60\%$) for the MIRI devices between 5 and 10 μm . We also model the cross-shaped artifact that was first noticed in the 5.7 and 7.8 μm *Spitzer*/IRAC images and has since also been imaged at shorter wavelength ($\leq 10 \mu\text{m}$) laboratory tests of the MIRI detectors. The artifact is a result of internal reflective diffraction off the pixel-defining metallic contacts to the readout detector circuit. The low absorption in the arrays at the shorter wavelengths enables photons diffracted to wide angles to cross the detectors and substrates multiple times. This is related to similar behavior in other back illuminated solid-state detectors with poor absorption, such as conventional CCDs operating near 1 μm . We investigate the properties of the artifact and its dependence on the detector architecture with a quantum-electrodynamic (QED) model of the probabilities of various photon paths. Knowledge of the artifact properties will be especially important for observations with the MIRI LRS and MRS spectroscopic modes.

Keywords: instrumentation: detectors – methods: numerical – space vehicles: instruments – techniques: image processing

1. INTRODUCTION

Developed in the 1980's (e.g., Petroff & Stapelbroek 1980, 1984, 1985; Stetson et al. 1986), arsenic doped extrinsic silicon (Si:As) Blocked-Impurity-Band (BIB - or Impurity Band Conductor - IBC) detector arrays are widely used in the field of mid-infrared astronomy. Mul-

iple space missions have made them their detector of choice due to particular attributes: their wide spectral region coverage (5-28 μm), high quantum efficiency, low dark current, stable performance for an extended period of time, low heat dissipation (which is particularly important for cryo-cooled space missions), and nuclear radiation hardness. The sizes and performance of arrays of these detectors have increased over time. The Short Wavelength Spectrometer on the Infrared Satellite Observatory (ISO), launched in 1995, utilized a 1 \times

12 array (Leech et al. 2003), the MSX satellite, launched in 1996, had 8×192 arrays (Mill et al. 1994), while IRS and MIPS on the Spitzer Space Telescope had 128×128 devices (Van Cleve et al. 1995) and the IRAC/Spitzer 5.7 and 7.8 μm (Hora et al. 2004) and the Akari (Onaka et al. 2007) arrays were 256×256 . The latest generation detectors are 1024×1024 , such as the 12 and 23 μm arrays of the WISE mission (Mainzer et al. 2008) and the three focal plane arrays (FPAs) (Ressler et al. 2008) mounted in the Mid-InfraRed Instrument (MIRI) of the James Webb Space Telescope (*JWST*).

Much of the theory on the operation of these detectors was published in the 1980’s, shortly after they were invented, i.e.: Petroff & Stapelbroek (1984, 1985); Stetson et al. (1986); Szmulowicz & Madarsz (1987); Szmulowicz et al. (1988). Since then there has been substantial progress in the detector quality, primarily through improved control of minority impurities, resulting in successful fabrication of devices with much thicker infrared-active layers than previously (Love et al. 2004). The original efforts are largely successful in describing the properties of these improved devices at the longer wavelengths. However, testing of detectors with these thicker layers showed that the behavior of responsivity vs. bias voltage requires introduction of a diffusion length of $\sim 2.5 \mu\text{m}$ (rather than the negligible diffusion length in the original theory), or the response at low bias and wavelengths near the peak of response would fall short of measurements (Rieke et al. 2015). This change is required because at wavelengths $\gtrsim 15 \mu\text{m}$, most of the photons are absorbed in the first ~ 10 microns of the infrared-active layer. At low bias, the field does not penetrate across this layer and the photo-electrons must diffuse across a field-free zone to be collected and produce a signal.

In addition, the detectors have been utilized down to wavelengths as short as $5 \mu\text{m}$, far from their peak response at 12 - 25 μm . Quantum Efficiencies (QE)¹ of $> 40\%$ are expected in the 5 - 8 μm range (Love et al. 2005; Woods et al. 2011). Such applications complement InSb and HgCdTe photodiodes that until recently have had high performance only at wavelengths short of $5 \mu\text{m}$. Most notable of these applications was the IRAC/Spitzer channel 3 and 4 detector arrays (Fazio et al. 2004; Hora et al. 2004), developed by Raytheon (Estrada et al. 1998). Pre-launch measurements indicated that the IRAC detectors reached a QE of 37% (following revisions after launch) and 56% at 5.6 and 8.0 μm , respectively (Pipher et al. 2004). However, on or-

bit the achieved performance fell short of expectations from these values; the equivalent instrument throughputs were only 45% and 61% of the pre-launch predictions, respectively. This discrepancy was traced to a substantial portion of the signal appearing over an extended region on the detector. This signal was included in the laboratory measurements that integrated over a large fraction of the array, but was excluded in the on-orbit measurements, which were analyzed with point-source photometry (Hora et al. 2004). This behavior raises a question about whether the expected QE was actually achieved.

On-orbit images with IRAC showed that this extended response appeared as an image artifact, which the IRAC publications termed “banding” (Hora et al. 2004; Pipher et al. 2004). The artifact can be described as a cross along the pixel columns and rows centered on the sources. Various tests were executed on a sister detector of the IRAC flight hardware at the University of Rochester to find the origin of the artifact (Pipher et al. 2004). External optical effects were ruled out by the placement of a dark mask around the laboratory pinhole, which did not mitigate the “banding.” Their tests also showed that the strength of the artifact increases with decreasing wavelength and that light is scattered not just into the bands, but also into the entire detector area. These results indicate that the artifact is not due to an issue with the readout electronics but is internal to the detector. The IRAC Instrument handbook (Laine 2015) describes the banding as a result of diffraction off the rectilinear grid of conductive pads and multiple scattering within the detector. This conclusion indicates that the behavior is similar to scattering observed in the near infrared with conventional CCDs (Gull et al. 2003; Ryon 2019); i.e., that it is a general issue with back-illuminated solid state detectors being operated in spectral regimes where they have poor absorption.

This paper complements the evaluation of the long wavelength behavior of Si:As IBC detectors described in Rieke et al. (2015). We will discuss both the short wavelength QE and the imaging artifacts. We start with a description of the detector architecture (Section 2). We then derive the wavelength dependence of the quantum efficiency and show good agreement with the behavior of the flight detectors for MIRI on *JWST*, including quantum efficiencies of up to $\sim 60\%$ in the 5 - 10 μm range for arrays with suitable anti-reflection coatings (Section 3). The remainder of the paper focuses on the cause and morphology of the spreading of images in the shorter wavelengths, i.e., the “banding,” or the more descriptive term “the cross artifact” (Section 4). The work and modeling in this paper will inform the on-orbit image

¹ QE is defined as the fraction or percentage of incident photons converted to electrons

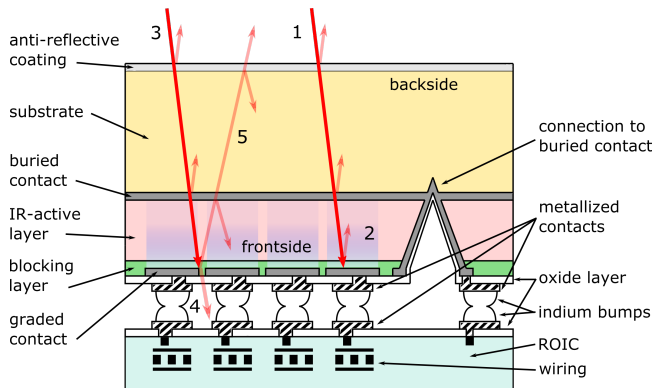


Figure 1. This drawing (not to scale) shows the general architecture of the MIRI Si:As arrays. Four pixels are shown with contacts and indium bumps to allow connection to their amplifiers in the readout integrated circuit (ROIC). The detector bias is established between the output contacts and the buried one. The individual electric fields of the four pixels are shown with a transparent blue gradient. The detectors are illuminated through their “backside”, i.e. through the substrate that supports them rather than directly into the detectors, i.e. the “frontside.” Two possible photon paths are also shown. Path (1) is the traditional fate of photons: they undergo reflective losses at the entrance and reflective and absorptive losses at the buried contact. If they are then absorbed in the IR-active layer, they create a photoelectron that traverses this layer and the blocking layer to be collected at a contact. Those that are not absorbed in the IR-active layer are reflected off the metallized contacts (2) and traverse the detector layers in reverse. Photons along path (3) have a similar trajectory but they are incident on a gap between the metallized contacts and either pass into the gap between detector and ROIC wafers (4) or are diffracted to wide angles (5), some of which are sufficiently off-axis to lead to total internal reflection and trapping within the detector wafer. These wide-angle photons may be detected far from the original input point.

analysis for MIRI, which will in turn be used to refine the models to enhance the calibration of this instrument, particularly of its spectrometers.

2. DETECTOR ARCHITECTURE

In Figure 1, we show the general architecture of modern Si:As IBC detector arrays. The detectors are grown on a substrate and illuminated through it. They consist of (1) a buried contact to establish an electrical field, (2) an IR-active layer that is heavily doped with arsenic to create an impurity band where the photons are absorbed, elevating free electrons into the conduction band, (3) a high purity layer that blocks dark current from the impurity band but allows passage of photoelectrons in the conduction band, and (4) an output contact. For the MIRI baseline arrays, the substrate is $420\ \mu\text{m}$ thick, the IR-active layer is $35\ \mu\text{m}$, and the blocking

layer is $\sim 4\ \mu\text{m}$. The substrate is of a high resistivity (i.e., low impurity content) silicon wafer. The arsenic impurity (a donor) in the IR-active layer has a concentration of $7 \times 10^{17}\ \text{cm}^{-3}$, while acceptor-type impurities are at a level of about $1.5 \times 10^{12}\ \text{cm}^{-3}$. This low level of the minority impurity is critical to allow the electric field (shown in blue shading in the figure) to penetrate the IR-active layer for complete collection of photoelectrons at a bias level that does not trigger avalanche gain (and the resulting increase in noise). The $\sim 4\ \mu\text{m}$ thick blocking layer just before the output contacts is of high purity and hence has no impurity band. As a result, it blocks thermal currents, while allowing free transit to photoelectrons, which have been elevated into the conduction band (which, of course, is continuous from the IR-active layer through the blocking one). When the photoelectrons reach the contacts, they are sensed by integrating amplifiers in the readout integrated circuit (ROIC), connected through indium bump bonding hybridization (i.e., cold welding of indium bumps deposited on the detector and the readout wafers).

Figure 1 also illustrates some fates for incident photons. There are reflective losses at the entrance to the substrate and both reflective and absorptive ones in the buried contact. Near the peak of response ($12 - 24\ \mu\text{m}$) close to all the photons that survive through these layers are absorbed in the IR-active layer, either in the first pass (downward in Figure 1) or after reflection from a metallized contact. However, a significant fraction of photons ($\geq 10\%$) that are not absorbed in the initial downward pass are lost within an inter-pixel gap, while others undergo diffraction due to the pixel lattice structure (the fraction of photons that diffract depends on the detector architecture and the wavelength of the photons). In the region of peak response, very few of these photons will get through the IR-active layer on their upward trajectory and are therefore most likely detected in the same pixel as they entered. However, if the IR-active layer has low absorption many of them will escape back upward into the substrate. Many of those will be sufficiently off-normal to undergo total internal reflection when they encounter the upper edge of the substrate, leading to their being trapped in the silicon. These photons are responsible for the large scale of the imaging artifact.

3. RESPONSE AND QUANTUM EFFICIENCY

Si:As IBC detectors can offer systems level advantages through their ability to provide good performance from 5 through $\sim 27\ \mu\text{m}$. To quantify this performance, in this section we consider the QE and response in the $5 - 10\ \mu\text{m}$ range, where the arsenic absorption coefficient is

less than the values at the peak of response from 12 – 20 μm . The low values of the absorption cross section between 5 and 10 μm have led to a presumption that the QE of the detectors would be low there. However, QEs of up to $\sim 60\%$ are achieved by the MIRI detectors; our model explores the parameters that make such high levels possible.

3.1. Modeling the response

Our model of the short wavelength response of Si:As IBC detectors uses the parameters of the MIRI “baseline” devices as described above and in more detail by Love et al. (2004, 2005, 2006); Ressler et al. (2008); Rieke et al. (2015); Ressler et al. (2015). We assume that the wavelength-dependent response is determined through a combination of (1) the absorption characteristics of the Si:As, (2) the anti-reflection coating on the entrance surface, (3) the optical characteristics of the buried contact, and (4) geometric factors.

There are a number of determinations of the absorption cross section of As in Si (Petroff & Stapelbroek 1985; Geist 1989; Woods et al. 2011). Geist (1989) shows that taking the cross section to be 0.7 times the formula provided by Petroff & Stapelbroek (1985) provides an excellent fit to the data between 500 and 750 cm^{-1} (13.3 – 20 μm). The Petroff & Stapelbroek (1985) fit follows a dependence of $\propto \lambda^{1.85}$ between 5 and 25 μm . However, Geist (1989) finds that the slope in the theoretical study of Coon & Karunasiri (1986) is steeper, as $\propto \lambda^{2.25}$. The measurements of Woods et al. (2011) are the only ones extending down to 5 μm (and below). They agree with those of Geist (1989) and Petroff & Stapelbroek (1985) in most of the region of overlap. They are inaccurate beyond 25 μm , failing to reflect the steep drop in sensitivity that begins at $\sim 27\text{ }\mu\text{m}$. However, the region from 5 – 15 μm is the range of interest for this paper. We show their results for these wavelengths in Figure 2 along with a fit proportional to $\lambda^{1.99}$.

Ijaiwi & Tomak (1990) show that the shape of the theoretically predicted absorption coefficient depends critically on the assumed potential describing the screening behavior of the impurities. However, their calculations agree very well with each other for the isotropic hydrogenic, Yukawa, and Hülthén potentials, all of which also agree with the $\propto \lambda^{1.85-1.99}$ behavior.

We consider the absorption coefficient to be well determined, therefore; to be specific, we have used the values from Woods et al. (2011). The errors on these values are estimated at 6% at 10 μm but much larger at 2 μm ; we have assumed between 5 and 10 μm they scale linearly, so they are 12% at the former wavelength.

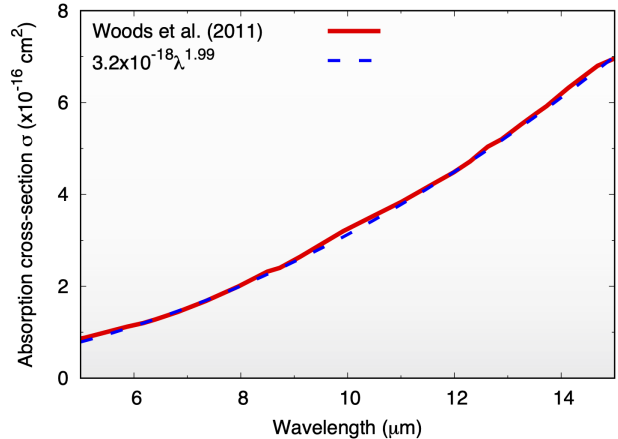


Figure 2. The absorption cross section for Si:As from Woods et al. (2011), along with a simple fit.

The MIRI arrays have one of two single-layer AR coatings of ZnS, in one case optimized for 6 μm and in the other for 16 μm . We have modeled the array where this coating is optimized for 16 μm , since the high absorption coefficient around this wavelength allows us to determine the effects of the buried contact unambiguously. We have taken cryogenic refractive indices for silicon from Li (1980) and for ZnS from Hawkins & Hunneman (2004). The predicted wavelength-dependent quantum efficiency shows two peaks, i.e., one at 16.3 μm corresponding to $\lambda/4$ and another at 5.8 μm for $3\lambda/4$ (the wavelengths do not differ by exactly a factor of three because of the wavelength dependence of the refractive indices). These values are a result of tuning the modeled thickness of the AR coating to provide the best match to the observed peaks, deriving a value of 1.95 μm (in good agreement with the measured value).

From early-on, it was recognized that the buried “transparent” contact was not fully transparent; Petroff & Stapelbroek (1985) estimated that it was 25% absorptive for one of their back-illuminated detectors. These contacts consist of a layer doped with a shallow impurity, such as arsenic, antimony, or phosphorus, so they show a decrease in absorption toward short wavelengths, just as photoconductive detectors based on such impurities do. The optical behavior of such contacts has been modeled by Hoelzlein et al. (1980) but is seldom included in modeling detectors. These models show that they both reflect and absorb incoming energy. We have obtained the absorptive component for typical contacts from M. G. Stapelbroek (private communication, see Figure 3). The fringing model described by Argyriou et al. (2020) indicates reflection at the level of $\sim 4\%$ from ~ 5 to $\sim 9\text{ }\mu\text{m}$ (beyond 9 μm , the detector absorption dominates the optical behavior). We have assumed 4% reflection

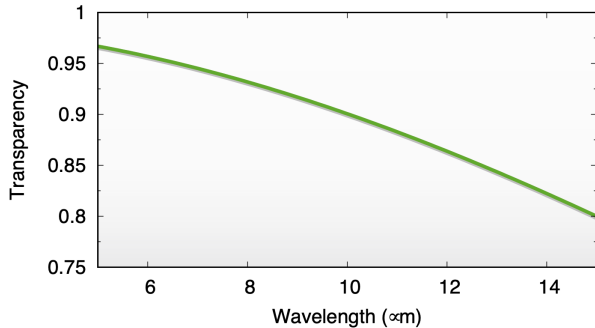


Figure 3. The absorptance of the buried contact. The plot shows that the buried contact is much more absorptive at the longer wavelengths. The higher transparency of the contact below $10 \mu\text{m}$ helps explain the relatively high QE at these wavelengths. The high transparency is also important for our modeling in Section 4.2.2, as it determines the fraction of photons that are able to travel through the buried contact multiple times and hence be absorbed in the IR-active layer and detected far from their entry point into the array.

at all wavelengths for the QE modeling (we ignore reflectance for the diffraction pattern modeling in the later part of the paper).

The primary geometric property affecting the detector quantum efficiency is the inter-pixel gaps in the backside contacts. The pixels are $25 \mu\text{m}$ square and have pixel-to-pixel gaps of $\sim 2 \mu\text{m}$. The model described below assumes that all photoelectrons freed in the infrared-active layer are collected at a contact because of the fringing effect on electric fields for closely spaced electrodes (e.g. Lisowski & Skopec 2009). However, photons that penetrate to the contacts are reflected back through the detector layer, where additional absorption adds to the photo-current. In our model, the reflected signal is decreased to match the areal coverage of the contacts. A small additional absorption occurs for photons reflected back from the buried contact or detector backside when they pass through the IR-active layer. The model will include a total of two complete passes through the detector (i.e. four passes through the IR-active layer).

A model was built combining these various effects. The absorption near $16 \mu\text{m}$ in the transparent contact was normalized to match the measured QEs. The resulting dependence of QE on wavelength is shown in Figure 4. The model provides a satisfactory fit to the measurements, and this fit is improved if the “high” values of the absorption coefficient are adopted at the shorter wavelengths, where high means those increased in accordance with the estimated errors in Woods et al. (2011). In this model, the buried contact absorbs 18% of the signal at $16 \mu\text{m}$, qualitatively similar to the values obtained previously.

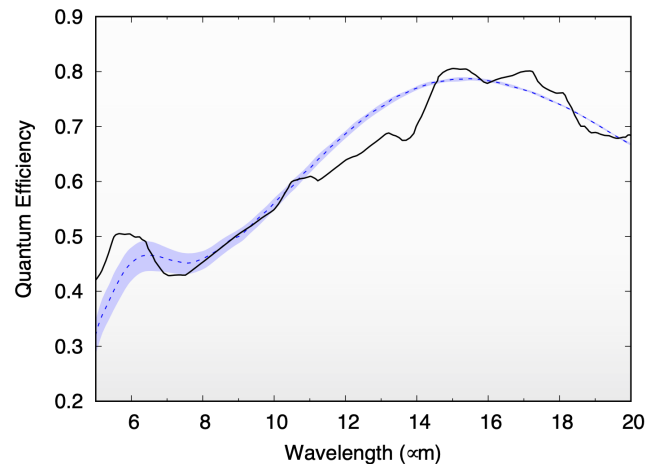


Figure 4. Measured wavelength-dependent quantum efficiency for the MIRI baseline detector array modified to include the calculated enhancement with the single-layer AR coating (solid black line, from Ressler et al. (2008)) compared with the prediction from our model (dashed blue line). The shaded area shows the errors of the model due to the uncertainties in absorption coefficients, taken to be $\pm 6\%$ at $10 \mu\text{m}$ and $\pm 12\%$ at $5 \mu\text{m}$.

The agreement of our model with the measurements of the detector array with a single-layer anti-reflective coating optimized for $16 \mu\text{m}$ demonstrates that the internal operation of the detectors is well understood for the $5 - 10 \mu\text{m}$ range. We therefore confirm that even higher QEs are expected in this range with a suitably optimized antireflective coating. Ressler et al. (2008) show a predicted value of $\sim 60\%$.

3.2. Detector gain?

The agreement between model and measurements in Figure 4 emerges in a straightforward way, based on a careful accounting of all the relevant effects. In an alternative approach, Woods et al. (2011) invoked detector gain at the wavelengths short of $10 \mu\text{m}$, i.e. a quantum yield > 1 .² We find that this is not necessary and is in fact unlikely. $\text{QY} > 1$ is improbable in extrinsic photoconductors (for photons below their bandgap energies)

² There are two common definitions of quantum yield (QY). In one, used by Woods et al. (2011), it describes the number of charge carriers produced per incident photon. In the other, which we prefer, there are two terms: (1) the QE is the fraction of incoming photons absorbed to produce free charge carriers, i.e., a peak of 0.78 or 78% in Figure 4, and (2) the QY is the average number of charge carriers produced per absorbed photon, i.e. ~ 1.66 at $5.6 \mu\text{m}$ in the Woods et al. (2011) analysis. Under their definition, the QY would be the QE multiplied by the QY as we define it. In our definition, the detector noise can be as small as the square root of the product of the photon flux and the QE, and $\text{QY} > 1$ leads to extra noise terms.

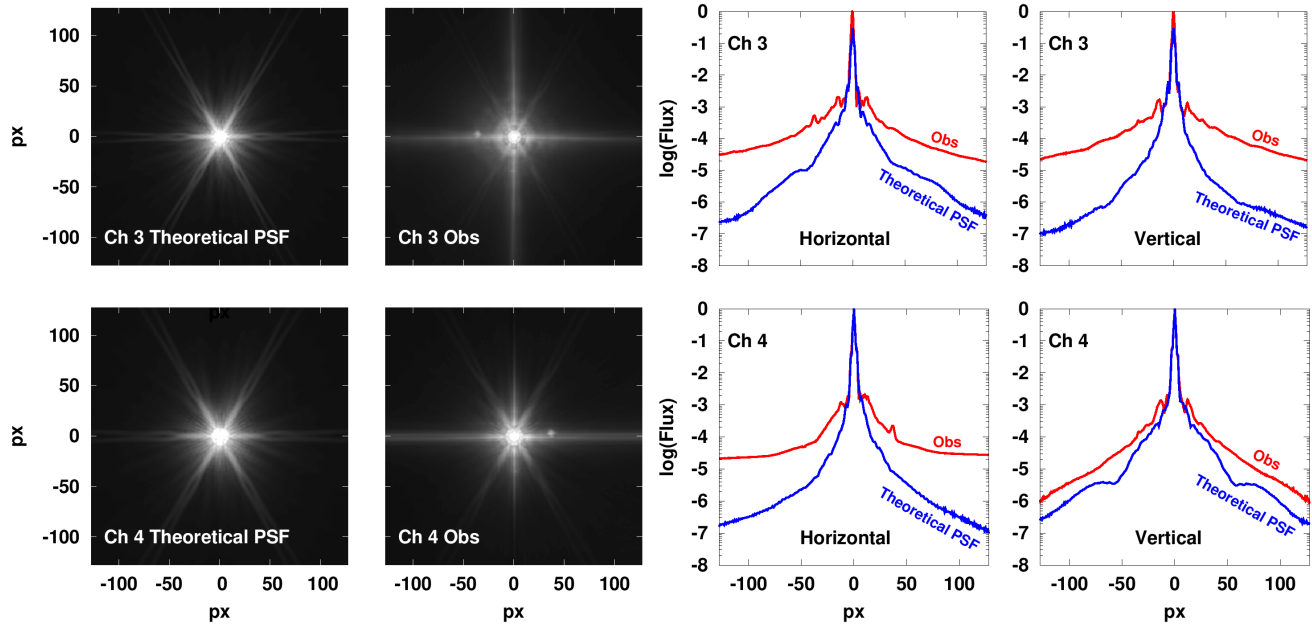


Figure 5. The cross artifact (or “banding”) is very apparent in the observed Ch 3 ($5.7 \mu\text{m}$) and 4 ($7.8 \mu\text{m}$) IRAC in-flight PSF images (downloaded from the Spitzer Science Center website). The artifact is not present in the STinyTim theoretical PSFs (John Krist), which includes the diffraction from the optical elements up to the focal plane of the instrument. The images on the *extreme left* show the theoretical PSFs, the following columns the observed PSFs, while the plots on the *right* show the pixel values along the rows and columns centered on the source. The artifact contrast is higher in the Channel 3 data and not as apparent in the vertical columns at Channel 4 as they are for the horizontal rows due to a “pullup” effect (see Hora et al. 2004, for details).

because the impurities that need to be ionized are so dilute in the crystal. In addition, gain in these detectors would be associated with increased noise above the simple square root of the number of absorbed photons. Two effects are relevant: (1) the excess electrons over those for $QY = 1$ are not independent; the number of independent events is the number of absorbed photons, not the number of resulting photoelectrons; and (2) the statistical fluctuations in the number of photoelectrons produced per photon means that the noise will be increased further. As an example of the first effect, at $5.6 \mu\text{m}$, Woods et al. (2011) predict $QY = 1.66$; therefore the number of independent absorbed photons will have been overestimated by this factor. Assuming the signal to noise ratio (SNR) goes as the square root of the number of absorbed photons, the SNR will be overestimated by a factor of 1.29. We simulated the second effect with a Monte Carlo calculation. This calculation allowed each simulated photon to produce 1, 2, or 3 photoelectrons and calculated the resulting signals as a 1000 second integration sampled every 3 seconds (analogous to the operation in MIRI). The resulting integration ramp was fitted by linear regression and the results compared as a function of the QY. For $QY = 1.66$, the prediction from this simulation is that the noise should be increased a

further factor of 1.14. That is, the value of the QY found by Woods et al. (2011) implies that the noise at $5.6 \mu\text{m}$ should be elevated by a total factor of $1.29 \times 1.14 = 1.47$ over that estimated from the square root of the number of collected charge carriers.

This prediction has been compared with the measured noise from the MIRI detectors. We used calibration data obtained in the *JWST* Cryo-Vacuum Test 3 (CV3) to determine the noise. A series of measurements was taken in each imager filter (except $25.5 \mu\text{m}$), with the total collected electrons adjusted to be approximately the same in all cases. These data were reduced to a series of images. Adjacent images were differenced to remove non-ideal behavior (e.g., reset anomaly, drifts) and photometry was conducted on the resulting images using a pseudo-aperture approach in which the “source” region is square and the “sky” is a surrounding square with the center removed, with all dimensions an integral number of pixels. The “signal” is then the total counts from the “source” minus the predicted number of counts adjusted to the same number of pixels from the “sky”. This extraction unit was placed randomly (except it was always centered on a pixel) over the difference image to obtain a Monte Carlo set of noise measurements. This geometry allows very straightforward calculation of the

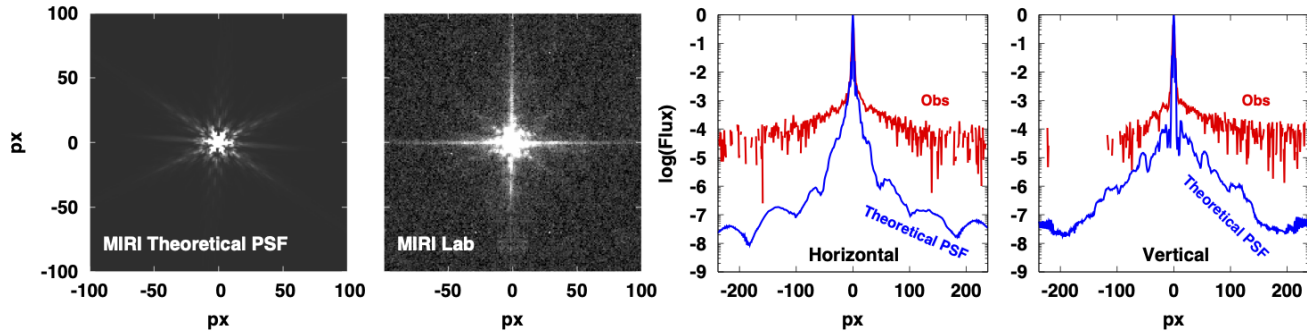


Figure 6. *Left panels:* The MIRI PSF generated with WebbPSF v. 0.8.0 (Perrin et al. 2012, 2014) at $5.6 \mu\text{m}$ and a PSF mask image taken with the MIRI flight detector during CV2 (second cryo-vacuum). The cross artifact is easily identified in the observed images (additional artifacts related to the laboratory setup have been artificially removed from the image for clarity). The cross artifact can be traced up to at least ± 400 px in the high contrast laboratory image. *Right panels:* The row and column pixels along the cross in the laboratory and modeled PSFs. The diffractive pattern increases the PSF flux by 3 orders of magnitude along the cross, up until it disappears in the background noise.

expected noise since both source and sky contain an integral number of pixels. We found a modest degradation of the detector noise behavior toward short wavelengths, by a factor of 1.15 at $5.6 \mu\text{m}$. This effect could have a number of possible causes; for example, instability in the source temperature will modulate the output flux more at the short wavelengths than at the long ones. Assuming the entire effect is true photon-noise-related, it is significantly less than predicted for the QY reported by Woods et al. (2011), i.e., the factor of 1.47 based on the photon statistics and our Monte Carlo simulation combined.

In the preceding section, we reproduced the full wavelength-dependent behavior of the MIRI detector quantum efficiency with $\text{QY} = 1$. Given this experimental evidence against values significantly above 1, we believe $\text{QY} = 1$ is correct for these devices operating at wavelengths $\geq 5 \mu\text{m}$.

4. “BANDING” OR THE “CROSS” ARTIFACT

A general issue for back-illuminated semiconductor photodetectors arises when the absorption efficiencies are low, allowing some photons to penetrate to the frontside from which they are scattered back into the detector array. Particularly if the array is thick, they can be absorbed and detected far from their point of entry. For example, for ACS on *HST*: “Long wavelength photons that pass through the CCD can also be scattered by the electrode structure on the [front] side of the device. This creates two spikes that extend roughly parallel to the x-axis. These spikes are seen at wavelengths longer than 9500 \AA in both the HRC and WFC” (Ryon 2019). Similarly for the STIS on *HST*: “Longward of 6000 \AA , the scattered light component becomes noticeable, pri-

marily due to scatter in the STIS CCD and climbs to a level of $\sim 10^{-3}$ at $10,000 \text{ \AA}$ ” (Gull et al. 2003).

A cross artifact due to this phenomenon at wavelengths $\leq 10 \mu\text{m}$ with Si:As IBC detectors was first noticed in the Channel 3 and 4 IRAC/*Spitzer* images (Pipher et al. 2004); see Figure 5. It can be described as a few rows and columns of bright pixels centered on a point source, with the artifact becoming brighter towards the source. The discussion below explores the causes of these internal scattering artifacts, focusing on Si:As IBC detectors, and demonstrates a theoretical simulation of them. That is, while Section 3 focused on the traditional type of response, trajectories (1) – (4) in Figure 1, we now focus on trajectory (5) and its further reflections. Since the analysis is computationally demanding, we simplify it by ignoring reflection at the buried contact, which is only at a $\sim 4\%$ level. Enabling reflection would significantly increase computational complexity by allowing a large number of additional photon paths, which would need to be tracked. Ignoring reflection at the buried contact has no significant effect on the results because it is an insignificant player in the response being modeled. We have verified this with a modification of our modeling code.

4.1. Details of the Si:As IBC detector behavior

In Figure 5, we show theoretical and in-flight observed point spread functions (PSFs) for the IRAC instrument, highlighting the considerable difference between the two. The *Spitzer* Science Center (SSC) pipeline notes that the artifact exhibits flaring and that narrow-band images have a more complex artifact pattern. Since IRAC had a dedicated detector at each wavelength and the PSFs could be well characterized, there were no addi-

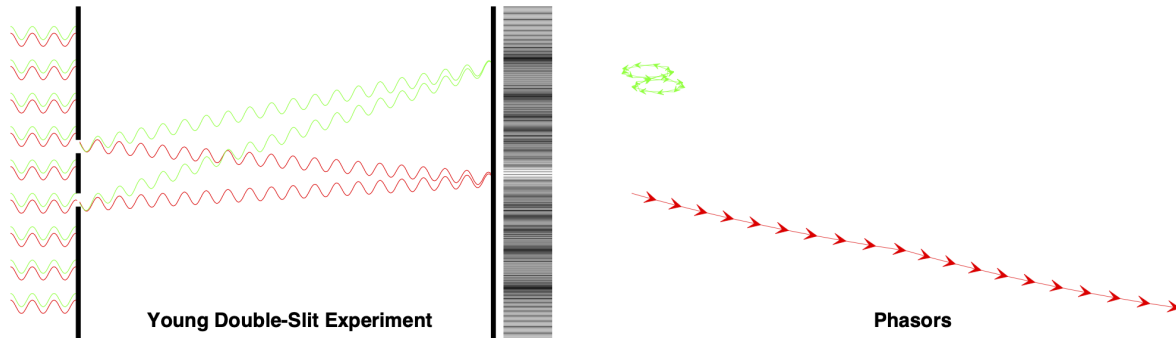


Figure 7. The Young double-slit experiment explained with Quantum-Electrodynamics. Random phasors add up at each imaging point and construct position dependent probability amplitudes. The square of the total probability amplitude at each position defines their relative intensities. As the image shows, at the peak of the intensity, the individual probability vectors add up to a large amplitude, while at the minimum they roughly cancel out and produce a small amplitude.

tional attempts to understand the nature of the artifact theoretically.

A similar “cross” also appears in the MIRI detector images. In Figure 6, we show the theoretical PSF calculated with WebbPSF v. 0.8.0 (Perrin et al. 2012, 2014) and images taken with the flight detector at the second cryo-vacuum test (with certain artifacts related to the laboratory setup artificially removed from the image), both at $5.6 \mu\text{m}$. Remarkably, the artifact is present out to at least ± 400 pixels in the high contrast laboratory images. As we show below, the artifact is a result of two optical properties of the detectors: 1) coherent light beams undergo diffraction off the metallic pixel contacts at the frontside of the detectors, and 2) inefficient photon absorption at shorter wavelengths ($\leq 10 \mu\text{m}$) in the IR-active layers and reflection off both the front and the back of the detector allows photons to travel through the detector multiple times. A pass through the detector and substrate three times (down, up, and down) produces an artifact extending to a maximum of ~ 200 px, meaning some of the $5.6 \mu\text{m}$ photons cross the MIRI detector at least two times to be detected at a distance of over 400 px. At 400 px the WebbPSF contrast is $\sim 10^{-9}$, while the standard deviation of the background in the CV2 data is at a contrast of $\sim 5 \times 10^{-5}$. The cross is 1σ above the background up to 150 px from the central source and is visually discernible to 400 px.

4.2. The Quantum Electrodynamic model of the detector

Since we were uncertain of details regarding the scattering/diffraction, we could not *a-priori* determine a simple specific model. Furthermore, our input light sources are more complicated than just a pinhole and realistic PSFs change as a function of wavelength. Therefore, we model the detector using the theory of Quan-

tum Electrodynamics (QED; Feynman 1948); as an all-encompassing Monte Carlo-style (MC) method it allows us to model aspects of the system we otherwise may have ignored.

4.2.1. Basics of QED

With QED modeling, all possible random directions of ray paths need to be explored, even if they violate classical optical laws. Each ray path carries its own probability amplitude and phase angle (or complex phasor), where the phase angle advances with traveled distance as

$$\Delta\varphi = 2\pi \frac{\Delta r}{\lambda}, \quad (1)$$

where λ is the wavelength of the tracer and Δr is the traveled distance. As the photons enter the silicon substrate from the outer vacuum their wavelengths shorten by a factor of $n_{\text{sil}} = 3.41$, i.e. a $5.6 \mu\text{m}$ photon will become a $1.64 \mu\text{m}$ photon. We quote the vacuum equivalent wavelength of photons in our work; however, the calculations use the appropriately shortened wavelengths. The phasors of unlikely paths cancel out, while the phasors of likely paths construct a large probability amplitude due to their similar phase angles. The resulting map of the square of the amplitudes yields the final relative probability of a photon being absorbed at a certain location and hence the intensity. In Figure 7, we explain the Young double-slit experiment with QED modeling, showing how the probability amplitudes at various locations add up. The total amplitude at the intensity peak is much larger than at the minima.

4.2.2. Tracer paths

We first describe how photons creating the cross artifact travel in the detector and then how the QED model describes the probability of each path. In Figure 1, we

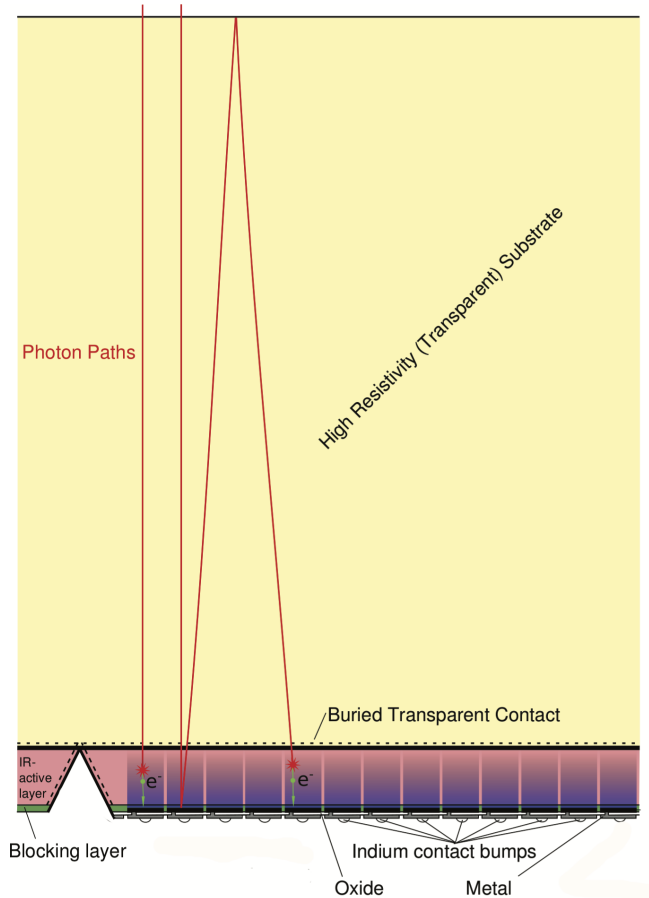


Figure 8. To-scale cross section of a detector array, illustrating how photons on trajectories similar to (5) in Figure 1 can be returned to array pixels far from their original entry points by total internal reflection at the array backside. The large thickness of the transparent substrate (relative to the IR-active layer and pixel sizes) enables photons diffracted at even smaller angles to be later absorbed at pixels offset from their entry point.

showed two possible paths with minor variations. In Figure 8, we show how diffracted photons ((5) in Figure 1) can be returned to the active pixels by total internal reflection off the array backside. We expand on this figure and show the most likely 10 paths a photon may take in Figure 9, with the probabilities of each path noted in Table 1. Paths 1 – 6 are variations of those from Figure 1, but paths 7 – 10 illustrate the cases for photons trapped by total internal reflection and show how they may travel many pixel widths within the detector array before being absorbed, detected, or lost. This process is relatively efficient because of the good transparency of the buried contact at short wavelengths as shown in Figure 3. Although theoretically there are an infinite number of possible paths for the photons to take

Table 1. Various path types in the detector at $5.6 \mu\text{m}$; nomenclature based on Figure 9. The statistics is based on our best estimates for detector parameters; there will be deviations from these statistics depending on their exact values.

Path ID	Description	Percent
Losses		
1	Exit at the side of the detector	0.11%
2	Exit in the pixel gap	9.39%
3	Absorption at the buried contact	1.03%
4	Exit at the top of the detector	1.79%
Detections		
5	Absorption in 1 st pass	27.09%
6	Absorption in 2 nd pass	35.63%
7	Absorption in 3 rd pass	11.91%
8	Absorption in 4 th pass	7.68%
9	Absorption in 5 th pass	2.56%
10	Absorption in 6 th pass	1.65%

NOTE—The sum of all losses and the eleven most probable detected tracer paths encompass 99.98% of all possible paths. Tracer path IDs larger than 10 are not shown in Figure 9; they are simply further crosses across the detector. Surprisingly, $\sim 11\%$ of the photons/tracers are lost through various modes. The first two detection paths will remain close to the image core and contain $\sim 63\%$ of the total flux (the detection within the second passing - path #6 - is higher than in the first, due to increased pathlengths from off-axis diffraction). Around $\sim 26\%$ of the total flux will be spread out (i.e. not absorbed in the first two crossings of the IR active layer), remaining in the detector and raising the “background” signal or contributing to the cross artifact. Our model ignores an $\sim 4\%$ reflection at the buried contact.

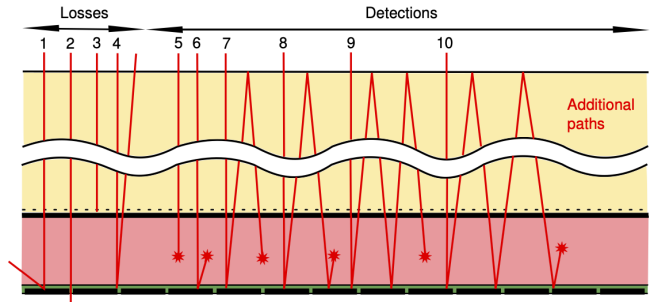


Figure 9. 10 most probable paths for a photon in the detector.

through the detector, 99% of the photons will travel on the most probable dozen or so path-types (see Table 1).

When describing the QED model, we use the word “tracer” to describe a particular photon path that is explored. We do this to differentiate it from paths that photons are more likely to take. Each tracer enters the detector with the same initial phase angle and unit amplitude. The total path length covered by the tracers is cumulatively monitored and used to calculate the phase angle when and if they are absorbed. As a tracer travels through the buried contact, it may either get absorbed (and vanish from the calculation) or transfer through it, according to the absorptance illustrated in Figure 3. As noted previously, we ignore reflection at the buried contact, due to its low probability and the computational simplifications this allows. The tracer then travels through the IR-active layer and either gets absorbed or survives its passage. The probability of absorption is described as

$$P_{\text{abs}} = 1.0 - \exp(-\alpha r) , \quad (2)$$

where r is the distance traveled in the IR-active layer and α is the absorption efficiency, which we derive from the fitted QE, i.e. the values as shown in Figure 2 adjusted to optimize the fit as in Figure 4. In Figure 10, we show how the probability of absorption increases for 5.6 μm wavelength photons with the cumulative distance traveled in the IR-active layer.

The total length that is travelled through the IR-active layer will depend on the incidence angle of the tracer, which is practically 0° for the first passage (ignoring minor variations due to OTA diffraction). If a tracer survives, it will get reflected off the metallic contacts at a random angle or disappear in the pixel gaps between the metallic contacts. Since in this section we are modeling the diffraction pattern, and the only surface yielding one is the pixel lattice, we generate new random directions for the tracers only at the metallic contacts and evolve them following regular reflection laws at the reflecting surface (hence the unusual reflection angle for the paths in Figures 1 and 9). This allows us to calculate the model with a “reasonable” number of photons. A reflected/diffracted tracer will assume its new direction and continue to travel toward the detector backside, with similar physical considerations as on the way from the backside to the frontside. For incidence angles larger than 0° , the travelled length will increase and therefore so will the absorption probability (see Figure 10) in the IR-active layer. The final fork in the road traveled by a tracer is at the backside, where it will either exit the detector or be reflected and repeat the previous cycle. Whether a tracer reflects or not depends on its incidence and polarization phase angles, and the probability is given by the Fresnel equations. If the incidence

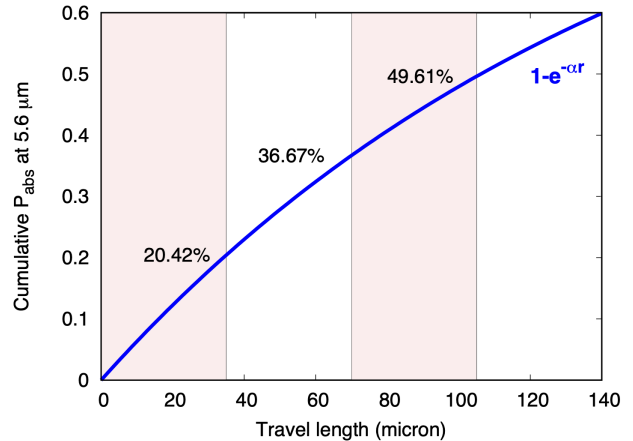


Figure 10. The cumulative probability of a 5.6 μm photon being absorbed in an Si:As IR-active layer as a function of travel length. The layer depth (35 μm) of the MIRI detector is shown and the probabilities of absorption marked for each full crossing of the IR-active layer. As the plot shows, even 2 full crossings does not guarantee a 50% absorption probability for a 5.6 μm photon (this statistic obviously does not take into account the fact that the diffraction pattern will force photons to travel diagonally across the active layer, thereby increasing the travel lengths and their absorption probabilities for each crossing). However, a 17.8 μm photon will have an over 90% probability of absorption in a single crossing.

angle is larger than the critical angle of total internal reflection

$$\Theta_{\text{crit}} = \text{asin} \left(\frac{1}{n_{\text{sil}}} \right) = 17.04^\circ , \quad (3)$$

then the tracer reflects with a nearly 100% probability (since the AR coating is virtually lossless). If this incidence angle is less, then we need to apply the Fresnel equations. Since most astronomical objects are not polarized, the model picks a random polarization angle and calculates a reflection probability. In Figure 11, we show the reflection probabilities of 50,000 tracers in the code, highlighting the large range of probabilities considered for the majority of incidence angles.

Since the patterns will likely form on spatial scales proportional to the input wavelength (which is reduced by a factor of n_{sil} once the photon enters the silicon detector), we divide each pixel into sub-pixels and calculate the phasor amplitudes as if the photons were absorbed in the center of the sub-pixels. The default setting of the model is to use 1 μm sub-pixels, which is close to Nyquist sampling the 1.64 μm wavelength of a 5.6 μm input photon after it enters the silicon. The model can also divide the IR-active layer into sub-layers, although this division has little effect. Absorption is calculated in the center of the sub-layers; if a single absorptive layer

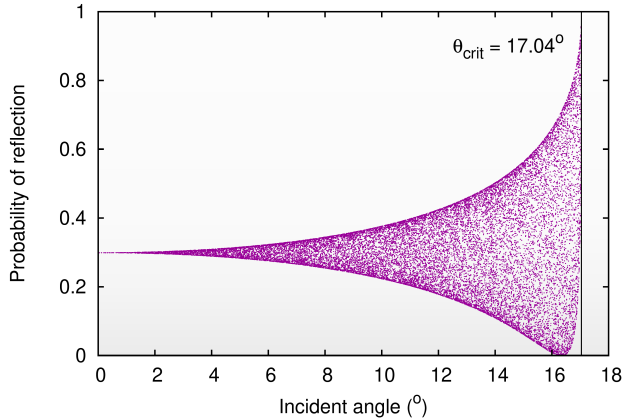


Figure 11. Reflection probabilities at the top (“backside”) of the detector for 50,000 tracers returning back after reflecting off the metallic pixel contacts. At incidence angles larger than the critical angle of total internal reflection all tracers will remain within the detector wafer, however, tracers with smaller incidence angles will either reflect or exit the detector, depending on their random polarization angle. If an astronomical source is emitting polarized light, there will be offsets from our general prediction.

is assumed (as in the default setting), then absorption is projected to occur in the middle of the IR-active layer.

4.2.3. Image flux scaling

We sample tracers from the square root of the initial intensity distribution and track the position and phase of their phasors as they travel in random directions. Sampling from the square root of the intensity distribution is necessary, as photon probabilities (i.e. intensities) are defined as the square of the total phasor amplitude. Therefore, to select unit amplitude tracers with correct probabilities, we need to sample them from the square root of the input intensity distribution. If a tracer is absorbed, we add its phasor to the total phasor in the respective sub-pixel it was absorbed in. When choosing from an input image or Airy ring, spatial positions are determined randomly based on cumulative flux distributions, thereby selecting brighter input positions more frequently than fainter ones.

We also need to track the number of tracers absorbed and initiated, as it is necessary to scale the relative probabilities. The vast majority of tracer paths are low probability, but their low probability needs to be established with a large number of test paths. Therefore, the model records each probable photon path type separately, being able to distinguish between the most probable photon paths. This is important because the final relative intensity map is calculated as the square of the phasor amplitudes, scaled by the total number of photons ab-

sorbed relative to the number of photons the model used. In equation form, the total intensity of a particular path at pixel position (x, y) would be described by

$$I_i(x, y) = \frac{N_i}{N_{\text{tot}}} \times \frac{A_i^2(x, y)}{\sum_j A_j^2}, \quad (4)$$

where N_i gives the total number of tracers absorbed in path i , N_{tot} gives the total number of test tracers used by the program, $A_i^2(x, y)$ the amplitude squared in pixel (x, y) for path i , while $\sum_j A_j^2$ is the total intensity captured with path i .

As many more photons are absorbed in the first photon passing, and probabilities are calculated as relative differences between sums, it would receive a significantly higher flux value if we did not correct for the number of photons each path (and layer) possibility (each with its own diffraction pattern) absorbed. This is an important aspect of QED; it calculates relative probabilities using sums. Furthermore, each absorption event is independent; there is no “interference” in QED in the classical sense (even though the final product is equivalent). Once a large enough number of tracers has been recorded for each possible path and absorption layer, we calculate intensity maps for each path-type and sum them up per pixel. Finally, the intensities of all path-types are summed for the total intensity per pixel.

4.2.4. Our modeling code GimMIRI

Unfortunately, MC algorithms are notoriously slow to converge, therefore our modeling code utilizes graphical processing units (GPUs). GPUs, with their parallel processing capabilities, provide an ideal environment for calculating the trajectories of independent tracers; hence they are widely used in ray tracing applications. We opted to encode our model using the Nvidia CUDA language, since the University of Arizona has a substantial Nvidia GPU cluster server³ and we have also received an academic hardware donation directly from Nvidia. The code we developed, called GimMIRI (GPU image for MIRI), is a multi-GPU single-node program written in C/CUDA, allowing it to use as many GPUs as are available (or requested) on a single computer node.⁴ The model only has a few basic input variables and a multitude of tweakable detector parameters that are defined and hard-coded in the source. The calculations are done at a single wavelength (which is one of the input variables) for each execution of the code and therefore if an extended bandpass is studied, multiple models need

³ <https://elgato.arizona.edu/>

⁴ Download from <https://github.com/merope82/GimMIRI>

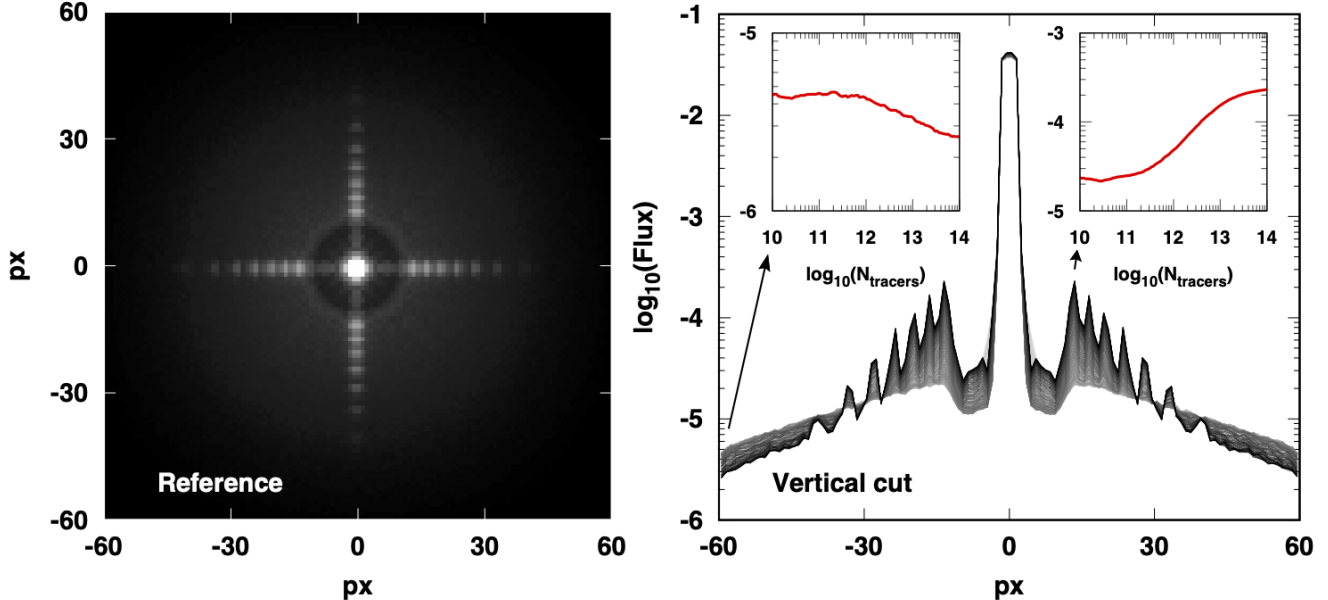


Figure 12. *Left panel:* Reference model GimMIRI image using a $50 \mu\text{m}$ radius pinhole as input flux distribution at an input wavelength of $5.5 \mu\text{m}$, modeled with 10^{14} tracer phasors. The variables of the Reference model are listed in Table 2. The cross artifact is apparent as well as a large halo. *Right panel:* The pixel values in the Reference model across a vertical cut centered on the pinhole. The flux values are shown for models between 10^{10} and 10^{14} tracers, with the lines getting darker for larger model tracer values. The convergence of the flux distribution for pixels (at rows -60 and 14) is shown in the sub-panels. A concrete criteria for convergence was not set; images were examined on a case-by-case basis. For the reference model, the two example pixels shown have levelled off to a similar relative variation of $10^{-16}/\text{tracer}$. With two differently illuminated regions (offset by an order of magnitude in flux) fluctuating around a similar low level of variation, the reference model was determined to have mostly converged at 10^{14} tracers, which took 59 hours of calculation time on two Nvidia TITAN BLACK GPUs.

to be run and their results co-added. The user can select between three flux input distribution types: 1) any fits file of their liking, 2) a pinhole of chosen radius, or 3) an Airy function (specified by the observing aperture). If a WebbPSF (Perrin et al. 2014) PSF fits file is used as input, the code sets the wavelength and oversampling rate for the calculation from the image header (which can be overwritten). Other than output frequency and naming options, the only variable the user sets for the compiled code is x and y pixel offsets.

Each individual CUDA thread calculates the path of a single tracer, generating numerous independent random numbers during the calculations: assigning new random angles of propagation at the metallic contacts, deciding whether a tracer is absorbed in the IR-active layer or the buried contact, and setting reflection probabilities based on random polarization angles at the backside of the detector. To ensure that each thread generates independent random numbers, all threads on all cards have their unique random generator seed that is stored on the graphical cards. Up until absorption, all threads calculate independently, and upon absorption an atomic addition process (serialized) adds the tracer phasor val-

ues to the specific sub-pixel’s cumulative value. Since it is not likely that two threads will add to the same exact subpixel, the atomic addition does not slow down the code. At requested intervals the code writes a new fits image, with the image header containing all relevant information.

4.2.5. Variables of the model

The variables of the model define the detector architecture, the finesse of the calculation, and the size of the output image. In Table 2, we define these variables and their values used in our reference model. Since the exact values of some of these variables are not available, we use reasonable assumptions for the MIRI detector. We execute a Reference model at $5.5 \mu\text{m}$, assuming a $50 \mu\text{m}$ radius pinhole as input flux distribution. While the pinhole is obviously not representative of an actual PSF, its simplicity and concentrated light allows our model to converge faster and enables a clearer study of each detector parameter. In Figure 12, we show our Reference model image.

4.3. Exploring the parameter space

Table 2. Variables used in the Reference model.

Variable	Description	Value
D_{act}	Width of IR-active layer	35.0 μm
D_{top}	Total height of detector	500.0 μm
s_{gap}	Pixel gap size	2.0 μm
s_{px}	Pixel pitch	25.0 μm
s_{sub}	Sub-pixel size	1.0 μm
λ	Input wavelength	5.5 μm
r_{pin}	Pinhole radius	50 μm
N_{path}	Number of paths considered	9
N_{lay}	Number of IR sub-layers	1
n_{sil}	Refractive index of material	3.4127
N_x	Output image size in x	120
N_y	Output image size in y	120
Θ_{off}	Offset in incident angle (normal)	0.045°
Γ_{off}	Offset in incident angle (CCW)	-13.75°

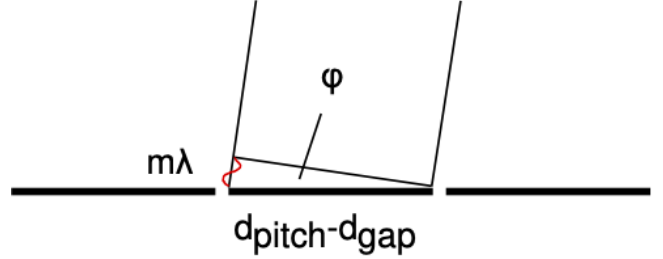
The diffraction pattern that is imaged depends on the various geometric parameters of the detector and the observed wavelength. As a first order approximation, the classic wave interference explanation of diffraction can help place each of them in context. In Figure 13, we display the direction of two beams at the top of a pixel-defining metallic contact, where the two beams constructively interfere at the $m = 1$ order. Based on this interpretation, one would expect constructive interference, where

$$m\lambda = (d_{\text{pitch}} - d_{\text{gap}}) \sin\varphi. \quad (5)$$

In the far field extreme, the two beams meet at infinity and the pixel offset can be calculated as

$$\Delta P = 2 \frac{D_{\text{top}}}{s_{\text{px}}} \tan\varphi. \quad (6)$$

Since the height of the detector (D_{top}) is only 20 times that of the lattice length (and around 300 times the wavelength), the far field approximation is not necessarily adequate for modeling, but we can use it for demonstration purposes. For the reference model, the pixel offsets of the $m = 1$ through 10 order peaks are at 2.8, 5.7, 8.6, 11.7, 15.0, 18.5, 22.5, 27.1, 32.5, and 39.3 pixels, according to the far field approximation. In fact, we see peaks in the diffraction pattern for the reference model at $\Delta P = 13.4, 16.5, 19.6, 23.5, 27.9, 33.0,$ and 39.6 pixel offsets, corresponding to the $m = 4$ to 10 orders. The $m = 1, 2, 3$ orders fall inside the critical angle of total internal reflection and are therefore not produced at a high contrast level. The agreement between the far field approximation and model results is worse for the

**Figure 13.** The classic wave interference explanation for diffraction off a periodic lattice.

lower orders, as the pathlength of the rays is shorter for them. For $m \geq 6$, the difference is less than a pixel for the reference model. Obviously, the level of agreement will depend on the detector architecture and the wavelength of observation. At $m = 15$, the diffraction angle would be larger than 90° and therefore it is not physically plausible; the $m = 14$ diffraction angle is 78.8° and the pixel offset is $\Delta P = 202.2$ px. This calculation also shows that any artifact that extends over this distance must be produced by more than a single reflection off the metallic contacts.

We modeled the diffraction pattern as a function of varying values for the pixel pitch (s_{px}), the pixel gap (s_{gap}), the input wavelength (λ), the detector substrate height (D_{top}), the size of the pinhole radius (r_{pin}), and the width of the IR-active layer (D_{act}). In Figure 14, we show the GimMIRI image as a function of these variables. The details of the pattern change, but the overall pattern remains and is dominated by the diffraction off the square grid of contacts. Other dominant patterns would result from other contact geometries.

We conducted a number of tests to be sure of the validity of our models. We checked for numerical convergence in Figure 12. The GimMIRI reference model is converged by 10^{14} tracer phasors. When modeling realistic PSFs, more tracers are necessary, therefore we will check for convergence again when modeling the *JWST* PSF responses at higher fidelity. We also checked dependence on the sub-pixeling and the number of sub-IR-active layers we model. Nyquist sampling with sub-pixeling is critical, however, sub-layering the IR-active layer is not as important, as long as absorbed photons are projected to be absorbed in the center of the layer.

5. VERIFYING OUR QED MODEL

We verify our QED diffraction model against the artifact pattern observed in the MIRI CV2 tests. For this test, we used the WebbPSF model of MIRI at 5.6 μm as the input flux distribution. It models the complete *JWST* optical path up to the instrument focal plane, and therefore provides the ideal input flux distribution

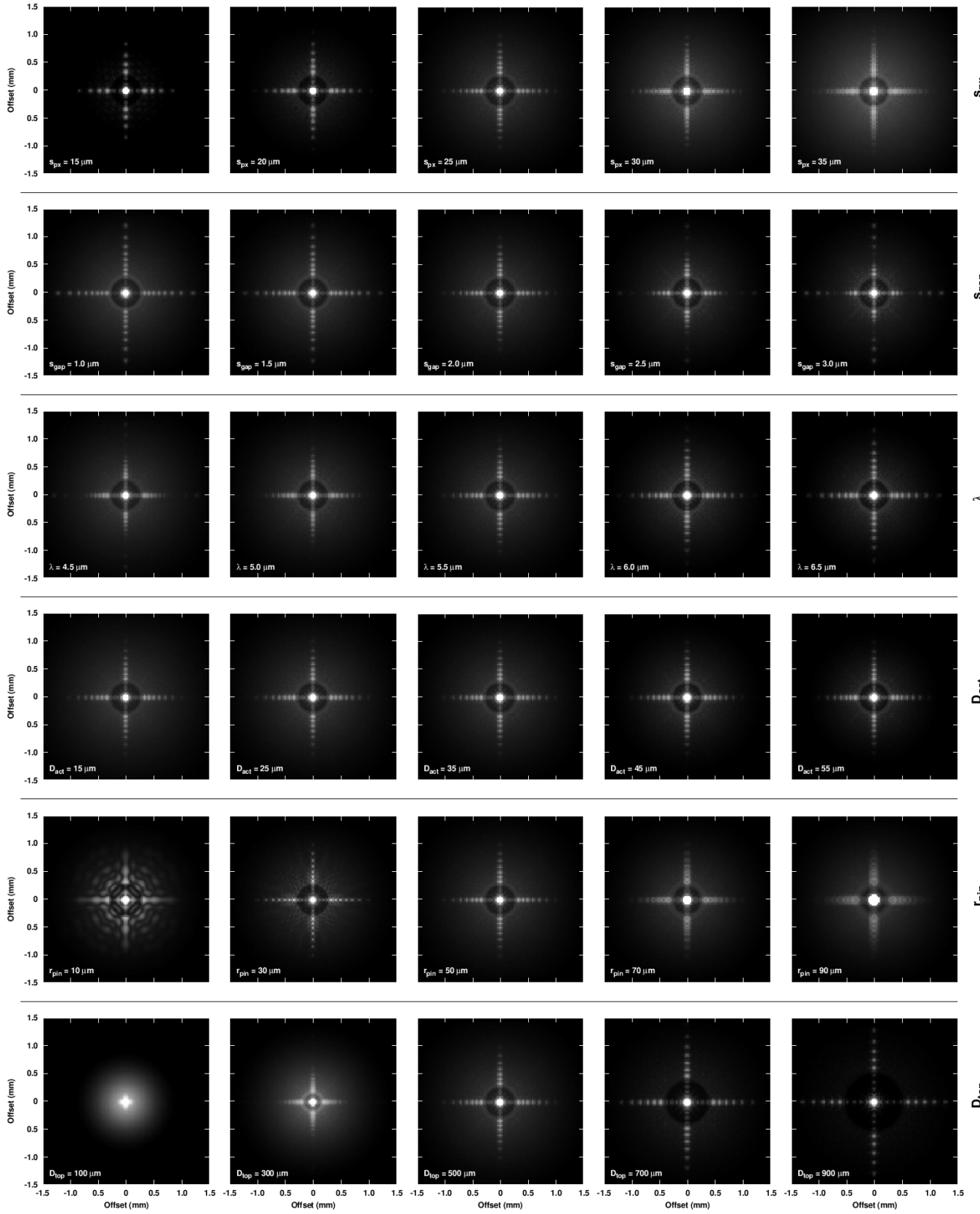


Figure 14. The diffraction pattern as a function of detector variables modeled with GimMIRI. The central column is the reference model. The variables are summarized in Table 2.

for our model. To simulate a realistic smooth input PSF, we used a 16 times oversampled WebbPSF model for our calculations. Calculating the GimMIRI image (to 10^{15} tracers) took a total of 1200 hours on two Nvidia TITAN BLACK GPUs.

The WebbPSF model has an integrated unit intensity (by definition), while the modeled GimMIRI PSF has an integrated intensity of 0.835. This shows that 83.5% of the incoming flux remains within the detector; the increase compared with the QE calculated for the central response only in Section 3 is an indication of the extent of the diffraction effects. The number is also slightly lower than the cumulative absorbed value given in Table 1, as the verification model “only” encompassed a $200 \text{ px} \times 200 \text{ px}$ area, resulting in higher losses at the detector edge. The peak intensity of the PSFs, however, scale by a factor of 0.624, which agrees with the QE values estimated by Ressler et al. (2008) and in Section 3 for a device with an AR coating optimized for $6 \mu\text{m}$. The difference between the two scalings highlight that a significant portion (21.2%) of the flux gets placed into both the diffraction spikes and into a halo surrounding the peaks, and also the problems posed by the artifacts when calibrating spectral data.

In Figure 15, we compare the theoretical *JWST*/MIRI PSF calculated with WebbPSF to the complete PSF calculated with GimMIRI, and with that measured using a flight hardware at the second cryo-vacuum tests (CV2). All images are at $5.6 \mu\text{m}$ (at native pixel scale). The cross artifact is apparent in both the observed PSF and the modeled one, although modeling with additional photon tracers would likely strengthen its signal in the final model image. The top row of Figure 15 shows the output GimMIRI PSF image and the WebbPSF model that was used as the input for the modeling, as well as their difference. The top-right panel highlights where the internal diffraction places the flux removed from the PSF core. The middle-row of Figure 15 shows the difference between the measured CV2 PSF and the WebbPSF model. It is clear that the WebbPSF is not adequate to model the observed diffraction structure. The bottom row of Figure 15 compares the CV2 image with the GimMIRI one. Our model removes the PSF core and most of the diffraction pattern, but not the complete structure. This is due at least in part to the fact that the laboratory image was taken using the F560W MIRI filter, which has a broad transmission window within 5.0 and $6.2 \mu\text{m}$, while the GimMIRI model is at a single wavelength. The broader transmission profile will result in a smooth diffraction spike, which the single wavelength model cannot replicate.

Our model reproduces the cross artifact produced by tracers up to path #8 in Figure 9, which can physically extend up to $\sim 200 \text{ px}$. The artifact can be traced further out at very low levels (see Section 4.1) in actual images. While our model does include these unlikely tracer paths, modeling constructive interference with QED tracers at those distances is very expensive computationally. Further work will be necessary to enable quicker (and possibly less accurate) modeling of the diffraction structure. Regardless, GimMIRI provides a complete model of all the attributes of the detector physics, thereby providing a baseline for future approximations.

6. SUMMARY

We have addressed two phenomena regarding the short wavelength ($5 - 10 \mu\text{m}$) performance of Si:As IBC detector arrays: (1) quantum efficiency; and (2) image artifacts. Our study confirms:

- Quantum efficiencies in the $5 - 10 \mu\text{m}$ range of $\sim 60\%$ are attainable with these detectors when suitably anti-reflection coated.
- This performance is achieved without quantum yields (QYs; i.e. the number of free charge carriers yielded per absorbed photon) > 1 . There should be no excess noise as would result if $\text{QY} > 1$.

At wavelengths of $5 - 10 \mu\text{m}$, these detectors show a large-scale cross-like imaging artifact. Related behavior is seen in other back-illuminated solid-state detectors where the absorption efficiency is low, e.g. conventional CCDs in the near infrared, allowing photons to scatter off contacts and other structures on the detector frontside. We show that

- The underlying cause of these artifacts is low absorption efficiency at the particular wavelength and diffraction off inter-contact gaps
- Photons can be diffracted to sufficiently large off-axis angles ($> 17^\circ$ in silicon) that they are totally reflected when they reach the detector backside.
- Consequently, these photons can be trapped in the detector/substrate wafer and can travel large distances until they are absorbed or escape, often leading to their detection far from their point of entry.

This research made use of Tiny Tim/Spitzer, developed by John Krist for the Spitzer Science Center. The

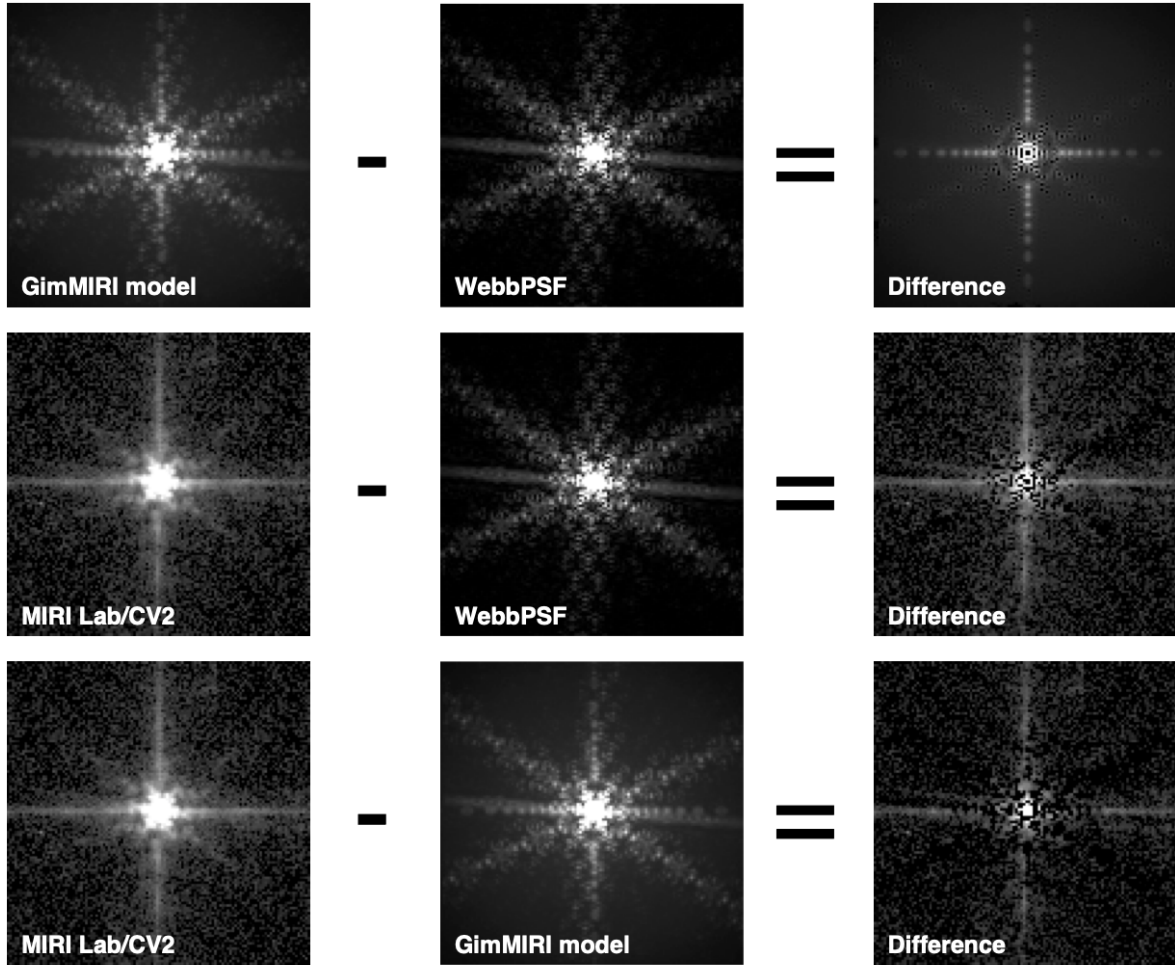


Figure 15. *Top Row:* Comparing the GimMIRI and WebbPSF model images at $5.6 \mu\text{m}$. The difference image highlights the location where the diffraction displaces $\sim 21\%$ of the incoming flux, mainly into the diffraction spikes and a broad halo. *Middle Row:* Comparing the observed CV2 image and the WebbPSF model image. The difference image is generally similar to the one above, although there are some discrepancies for the inner region and the cross artifact is of greater extent. *Bottom Row:* Comparing the observed CV2 image and the GimMIRI model. The difference image shows that the model reproduces most of the artifacts in the observed image. However, it under-represents the extent of the cross artifact and has some low-level remaining discrepancies in the inner zone. These remaining issues can be addressed by simulating the image for the full bandwidth of the filter rather than for a single wavelength and possibly by using more tracer particles or a model addressing just this region. All images are scaled linearly between intensity levels of 0 and 0.0005 (where the total intensity of the theoretical PSF equals 1 and peaks at 0.15 in its core). See more details on this figure in the text.

Center is managed by the California Institute of Technology under a contract with NASA. This material is based upon work supported by the National Science Foundation under Grant No. 1228509. We are grate-

ful for the generous hardware donation from the Nvidia Corporation.

REFERENCES

- Argyriou, I., Wells, M., Glasse, A., et al. 2020, *A&A*, 641, A150, doi: [10.1051/0004-6361/202037535](https://doi.org/10.1051/0004-6361/202037535)
- Coon, D. D., & Karunasiri, R. P. G. 1986, *PhRvB*, 33, 8228, doi: [10.1103/PhysRevB.33.8228](https://doi.org/10.1103/PhysRevB.33.8228)
- Estrada, A. D., Domingo, G., Garnett, J. D., et al. 1998, in *Proc. SPIE*, Vol. 3354, *Infrared Astronomical Instrumentation*, ed. A. M. Fowler, 99–108

- Fazio, G. G., Hora, J. L., Allen, L. E., et al. 2004, *ApJS*, 154, 10, doi: [10.1086/422843](https://doi.org/10.1086/422843)
- Feynman, R. P. 1948, *Rev. Mod. Phys.*, 20, 367, doi: [10.1103/RevModPhys.20.367](https://doi.org/10.1103/RevModPhys.20.367)
- Geist, J. C. 1989, *ApOpt*, 28, 1193, doi: [10.1364/AO.28.001193](https://doi.org/10.1364/AO.28.001193)
- Gull, T. R., Lindler, D., Tennant, D., et al. 2003, in *HST Calibration Workshop : Hubble after the Installation of the ACS and the NICMOS Cooling System*, 147
- Hawkins, G., & Hunneman, R. 2004, *Infrared Physics and Technology*, 45, 69, doi: [10.1016/S1350-4495\(03\)00180-4](https://doi.org/10.1016/S1350-4495(03)00180-4)
- Hoelzlein, K., Pensl, G., & Schulz, M. 1980, *Applied Physics*, 23, 7, doi: [10.1007/BF00899563](https://doi.org/10.1007/BF00899563)
- Hora, J. L., Fazio, G. G., Allen, L. E., et al. 2004, in *Proc. SPIE*, Vol. 5487, *Optical, Infrared, and Millimeter Space Telescopes*, ed. J. C. Mather, 77–92
- Ilaoui, K., & Tomak, M. 1990, *Journal of Physics and Chemistry of Solids*, 51, 361, doi: [10.1016/0022-3697\(90\)90120-5](https://doi.org/10.1016/0022-3697(90)90120-5)
- Laine, S., ed. 2015, *IRAC Instrument Handbook*
- Leech, K., Kester, D., Shipman, R., et al. 2003, *The ISO Handbook*, Volume V - SWS - The Short Wavelength Spectrometer
- Li, H. H. 1980, *Journal of Physical and Chemical Reference Data*, 9, 561, doi: [10.1063/1.555624](https://doi.org/10.1063/1.555624)
- Lisowski, M., & Skopec, A. 2009, *IEEE Transactions on Dielectrics and Electrical Insulation*, 16, 24, doi: [10.1109/TDEI.2009.4784548](https://doi.org/10.1109/TDEI.2009.4784548)
- Love, P. J., Beuville, E. J., Corrales, E., et al. 2006, in *Society of Photo-Optical Instrumentation Engineers (SPIE) Conference Series*, Vol. 6276, *Proc. SPIE*, 62761Y
- Love, P. J., Hoffman, A. W., Lum, N. A., et al. 2004, in *Society of Photo-Optical Instrumentation Engineers (SPIE) Conference Series*, Vol. 5499, *Proc. SPIE*, ed. J. D. Garnett & J. W. Beletic, 86–96
- Love, P. J., Hoffman, A. W., Lum, N. A., et al. 2005, in *Proc. SPIE*, Vol. 5902, *Focal Plane Arrays for Space Telescopes II*, ed. T. J. Grycewicz & C. J. Marshall, 58–66
- Mainzer, A., Larsen, M., Stapelbroek, M. G., et al. 2008, in *Proc. SPIE*, Vol. 7021, *High Energy, Optical, and Infrared Detectors for Astronomy III*, 70210X
- Mill, J. D., O’Neil, R. R., Price, S., et al. 1994, *Journal of Spacecraft and Rockets*, 31, 900, doi: [10.2514/3.55673](https://doi.org/10.2514/3.55673)
- Onaka, T., Matsuhara, H., Wada, T., et al. 2007, *PASJ*, 59, S401, doi: [10.1093/pasj/59.sp2.S401](https://doi.org/10.1093/pasj/59.sp2.S401)
- Perrin, M. D., Sivaramakrishnan, A., Lajoie, C.-P., et al. 2014, in *Proc. SPIE*, Vol. 9143, *Space Telescopes and Instrumentation 2014: Optical, Infrared, and Millimeter Wave*, 91433X
- Perrin, M. D., Soummer, R., Elliott, E. M., Lallo, M. D., & Sivaramakrishnan, A. 2012, in *Proc. SPIE*, Vol. 8442, *Space Telescopes and Instrumentation 2012: Optical, Infrared, and Millimeter Wave*, 84423D
- Petroff, M. D., & Stapelbroek, M. G. 1980, "Blocked impurity band detectors", Google Patents
- . 1984, *Proceedings of the Meeting of the Specialty Group on Infrared Detectors*, IRIA-IRIS, 2
- . 1985, *Proceedings of the Meeting of the Specialty Group on Infrared Detectors*, IRIA-IRIS, 3
- Pipher, J. L., McMurtry, C. W., Forrest, W. J., et al. 2004, in *Proc. SPIE*, Vol. 5487, *Optical, Infrared, and Millimeter Space Telescopes*, ed. J. C. Mather, 234–243
- Ressler, M. E., Cho, H., Lee, R. A. M., et al. 2008, in *Society of Photo-Optical Instrumentation Engineers (SPIE) Conference Series*, Vol. 7021, *Proc. SPIE*, 70210O
- Ressler, M. E., Sukhatme, K. G., Franklin, B. R., et al. 2015, *PASP*, 127, 675, doi: [10.1086/682258](https://doi.org/10.1086/682258)
- Rieke, G. H., Ressler, M. E., Morrison, J. E., et al. 2015, *PASP*, 127, 665, doi: [10.1086/682257](https://doi.org/10.1086/682257)
- Ryon, J. E. 2019, *Advanced Camera for Surveys Instrument Handbook for Cycle 27 v. 18.0*
- Stetson, S. B., Reynolds, D. B., Stapelbroek, M. G., & Stermer, R. L. 1986, in *Proc. SPIE*, Vol. 686, *Infrared detectors, sensors, and focal plane arrays*, 48–65
- Szmulowicz, F., Diller, J., & Madarasz, F. L. 1988, *Journal of Applied Physics*, 63, 5583, doi: [10.1063/1.340335](https://doi.org/10.1063/1.340335)
- Szmulowicz, F., & Madarasz, F. L. 1987, *Journal of Applied Physics*, 62, 2533, doi: [10.1063/1.339466](https://doi.org/10.1063/1.339466)
- Van Cleve, J. E., Herter, T. L., Butturini, R., et al. 1995, in *Society of Photo-Optical Instrumentation Engineers (SPIE) Conference Series*, Vol. 2553, *Proc. SPIE*, ed. M. S. Scholl & B. F. Andresen, 502–513
- Woods, S. I., Kaplan, S. G., Jung, T. M., & Carter, A. C. 2011, *ApOpt*, 50, 4824, doi: [10.1364/AO.50.004824](https://doi.org/10.1364/AO.50.004824)